

# Development and characterization of high-frequency resonance-enhanced microjet actuators for control of high-speed jets

Puja Upadhyay<sup>1</sup> · Jonas P. R. Gustavsson<sup>1</sup> · Farrukh S. Alvi<sup>1</sup>

Received: 17 August 2015 / Revised: 5 April 2016 / Accepted: 12 April 2016 / Published online: 7 May 2016  
© Springer-Verlag Berlin Heidelberg 2016

**Abstract** For flow control applications requiring high-frequency excitation, very few actuators have sufficient dynamic response and/or control authority to be useful in high-speed flows. Due to this reason, experiments involving high-frequency excitation, attempted in the past, have been limited to either low-frequency actuation with reasonable control authority or moderate-frequency actuation with limited control authority. The current work expands on the previous development of the resonance-enhanced microactuators to design actuators that are capable of producing high-amplitude pulses at much higher frequencies [ $\mathcal{O}$  (10 kHz)]. Using lumped element modeling, two actuators have been designed with nominal frequencies of 20 and 50 kHz. Extensive benchtop characterization using acoustic measurements as well as optical diagnostics using a high-resolution micro-schlieren setup is employed to characterize the dynamic response of these actuators. The actuators performed at a range of frequencies, 20.3–27.8 and 54.8–78.2 kHz, respectively. In addition to providing information on the actuator flow physics and performance at various operating conditions, this study serves to develop easy-to-integrate high-frequency actuators for active control of high-speed jets. Preliminary testing of these actuators is performed by implementing the 20-kHz actuator on a Mach 0.9 free jet flow field for noise reduction. Acoustic measurements in the jet near field demonstrate attenuation of radiated noise at all observation angles.

## 1 Introduction

In recent years, notable improvements have been achieved in understanding of the nature of turbulent flows that are commonly encountered in various aerodynamic and aeroacoustic applications. Advances in experimental techniques and computational tools have not only contributed to our knowledge of the complex flow physics but have also allowed us to leverage and manipulate certain flow features to our advantage. Due to this reason, the area of active flow control (AFC) has seen tremendous growth over the past couple of decades. In principle, AFC allows control-on-demand using actuators that are devices that interact with the flow by injecting mass, momentum, or energy into the flow (Cattafesta and Sheplak 2011). Numerous AFC devices have been developed to potentially mitigate various adverse effects that arise in different applications involving turbulent flows. Synthetic jets, plasma actuators, steady and unsteady fluidic microjets, piezoelectric actuators, and acoustic drivers are few of the many active control devices that have been developed and characterized in the past few decades. A review article by Cattafesta and Sheplak (2011) highlights some of the noteworthy AFC actuators and discusses their strengths and limitations.

AFC often seeks to produce significant modifications of the flow field using a small and localized control input. Small-amplitude perturbations produced by different actuators are often sufficient to control low-speed flows. However, due to much higher energy in the mean flow, increased background turbulence, and high instability frequencies, high-speed flows are more demanding and often do not respond to small-amplitude forcing. Therefore, effective control of high-speed flows requires actuators that are not only robust and easy to integrate, but also have a larger

---

✉ Puja Upadhyay  
pujaupadhyay@gmail.com

<sup>1</sup> Department of Mechanical Engineering, FAMU-FSU College of Engineering, Florida State University, 2003 Levy Ave, Tallahassee, FL 32310, USA

dynamic range with requisite control authority for various flow conditions—requirements that are not easily met by most actuators. For instance, high-speed free shear flows studied at the Florida State University include cavity flows, impinging jets, and free jets. These flow fields have frequency components ranging from  $\mathcal{O}(100\text{ Hz})$  to  $\mathcal{O}(10\text{ kHz})$  (Krothapalli et al. 2003; Zhuang et al. 2006; Worden et al. 2014). The objective of the current work is to design actuators that are capable of producing high-amplitude output at high frequencies [i.e.,  $\mathcal{O}(10\text{ kHz})$ ] to target a wide range of aforementioned high-speed flow fields. This paper particularly focuses on the design of high-frequency actuators suited for noise reduction in high-speed jets; however, the characterization results presented can be also used to assess the viability of these actuators in other high-speed flows. To this end, we design and characterize *two actuators with nominal frequencies of 20 and 50 kHz*. The actuator design frequencies are guided by the dynamics of high-speed free jets, which will be discussed in Sect. 1.1.

### 1.1 High-frequency (HF) actuators for noise reduction in high-speed jets

Over the past few decades, the role of large-scale coherent structures as the dominant source of noise has been widely investigated for both supersonic as well as subsonic jets. Mollo-Christensen (1963, 1967) was one of the first few to identify the coherent nature of the near pressure field and discuss the possible significance of the organized large-scale eddies in noise production. Crow and Champagne (1971) and Moore (1977), among others, clearly exhibited the presence of these structures in axisymmetric turbulent jets using flow visualization. Motivated by these findings, a large volume of research has (experimentally and/or theoretically) focused on the role of these large-scale structures in the far-field noise radiation in supersonic as well as subsonic jets (Armstrong et al. 1977; Fuchs and Michel 1978; Tam et al. 2008; Morris 2009; Reba et al. 2010; Cavalieri et al. 2013). These structures are non-compact acoustic sources that are primarily responsible for low-frequency noise radiation, and mainly dominate the aft angle directivity (Tam et al. 2008; Jordan and Colonius 2013). Therefore, one of the primary goals of AFC for jet noise control is to modify the evolution of these acoustically dominant large-scale structures to reduce the radiated noise.

In the past few decades, various active control methods have been employed in the form of steady and unsteady actuation to control jet noise. Steady control has been used with some success in the form of microjets (Krothapalli et al. 2003; Alkislal et al. 2007), fluidic chevrons (Laurendeau et al. 2006), fluidic inserts (Kuo et al. 2012), among others. Steady control often seeks to modify the evolution of large-scale structures by imparting streamwise vorticity

in the jet shear layer. Unsteady actuation, on the other hand, has the potential to excite the jet at various frequencies. The actuation frequencies are usually guided by the instabilities of the base jet flow. The instability frequencies in the jet generally scale with the local shear layer thickness. In the initial region of the jet, where the shear layer is very thin, linear stability studies have shown that the jet is unstable to high frequencies,  $St_\theta \sim 0.01\text{--}0.02$ , where  $St_\theta = f\theta/U_j$  is the Strouhal number based on the jet's initial momentum thickness,  $\theta$  (Michalke 1977, 1984). In the downstream region of the jet, where the shear layer scales with the jet exit diameter,  $D$ , the jet is mostly unstable to a lower range of frequencies. Crow and Champagne (1971) demonstrated that the maximum amplification of the perturbations occurs at frequencies that correspond to  $St_D \sim 0.2\text{--}0.3$ , also known as the 'preferred' mode of the jet.

Experiments involving excitation of high-speed jets in the order of the jet preferred mode or the initial shear layer instability frequencies are severely limited due to lack of actuators with high bandwidth and/or control authority. This is particularly a challenge at laboratory scales where the associated frequencies are much higher. For instance, for a Mach 0.9 jet ( $Re_D = 10^5$ ,  $D = 2\text{ in.}$ ), the shear layer instabilities based on the initial momentum thickness are approximately at 20 kHz (Uzun and Hussaini 2011). As such, most of the experiments investigating the effect of unsteady excitation on high-speed jets have been limited to low speed, low Reynolds number or high speed, low Reynolds number jets. Some of the work involving unsteady excitation of low-speed jets is summarized next.

Excitation on the order of jet preferred frequency has shown maximum receptivity of the jet column at the preferred frequency with increased turbulent fluctuation, mixing, as well as enhanced radiated far-field noise. This has been the case for jets with both laminar and turbulent initial boundary layers (Crow and Champagne 1971; Bechert and Pfizenmaier 1975; Moore 1977; Ahuja and Blakney 1985). In contrast, excitation on the order of the most amplified shear layer frequency or frequencies much higher than the preferred frequency produced different results depending on the state of the initial exit boundary layer. For a laminar boundary layer, Zaman and Hussain (1981) and Hussain and Hasan (1985) showed that excitation at  $St_\theta \sim 0.012\text{--}0.017$  suppressed turbulent fluctuations by suppressing the formation of large-scale vortices. Both of these studies independently suggested that excitation at these  $St_\theta$  produces a rapid growth of instability waves resulting in their early saturation and early breakdown, preventing the formation of energetic vortical structures. Kibens (1980) observed suppression in broadband far-field noise as a result of excitation at the shear layer instability frequency. On the other hand, jets with initially turbulent boundary layer have

not been consistently responsive to high-frequency control. Moore (1977) reported a small attenuation of far-field noise for a jet with a turbulent exit boundary layer, whereas Zaman (1985) observed no suppression. Hussain and Hasan (1985) and Vlasov et al. (1999) suggested that control should produce similar effects in jets with initially turbulent boundary layers, *if the excitation amplitude and wavelength are sufficiently large*. However, due to the lack of flow control actuators with appropriate control authority and bandwidth, effective implementation of high-frequency control on high speed, high Reynolds number jets has been severely limited. To our knowledge, experiments performed by Samimy et al. (2007, 2010) using Localized Arc Filament Plasma Actuators (LAFPA) are the only studies involving unsteady control of high-speed jets at high frequencies. For a Mach 0.9 jet, an increase in OASPL (2–4 dB) was observed for forcing Strouhal numbers  $St_{DF} \sim 0.2\text{--}0.5$ , whereas a decrease in OASPL (0.6–1 dB) was attained with higher forcing Strouhal numbers ( $St_{DF} \sim 1.5\text{--}3.5$ ).

In this paper, we present the design and characterization of two high-frequency actuators that are capable of producing supersonic microjets at 20 and 50 kHz (nominally) for noise reduction in high-speed jets. Previous developments of the REM actuators by Solomon (2010) have been used as a design guideline in this study. A major portion of this paper focuses on high-resolution flow visualizations and acoustic characterization of the actuator flow field. In-depth analysis of the dynamic response of these high-frequency actuators for various set of input parameters is performed. Finally, preliminary testing of these actuators is performed by implementing the 20-kHz actuator on a Mach 0.9 ( $Re_D = 6 \times 10^5$ ) free jet flow. This excitation frequency is approximately an order of magnitude higher than the jet preferred frequency. Brief acoustic results from the jet near field are presented to show the effect of control on noise. The primary object of high-frequency control is to inhibit the formation of large-scale structures which are known to be the dominant sources of noise. An overall suppression of turbulent quantities resulting in a favorable impact on radiated noise is expected.

## 2 Experimental setup

The experiments performed for this study were carried out at the Florida Center for Advanced Aero-Propulsion (FCAAP) at the Florida State University (FSU). The actuators are characterized with acoustic measurements and flow visualizations studies using a high-resolution microschlieren system. The following subsections elaborate on the actuator design and characterization. Implementation of the 20-kHz actuator on a Mach 0.9 jet flow was performed

in the STOVL high-speed jet facility at FCAAP. Details on actuator implementation are presented in Sect. 5.1.

### 2.1 Resonance-enhanced microjet (REM) actuator design

REM actuators are fluidic actuators based on aeroacoustic principles and utilize flow-acoustic coupling to produce pulsed supersonic microjets. Figure 1 shows the actuator schematic. The actuator design is fairly simple and consists of a cylindrical cavity with an orifice at the bottom. A converging source nozzle of diameter  $d$ , supplied by compressed nitrogen, is used to produce a source jet where the underexpansion ratio can be varied. This underexpanded source jet impinges upon the actuator cavity, producing high-amplitude pressure fluctuations in the cavity and a pulsed supersonic microjet from the orifice, under suitable flow and geometric conditions. Actuator frequencies depend on the incoming source jet conditions as well as geometric parameters ( $V$ ,  $L_c$ ,  $d_c$ ,  $L_m$ ,  $d_m$ ,  $h$ ) defined in Fig. 1.

REM actuators produce supersonic microjets at *discrete frequencies* when the cavity entrance is situated in the pressure recovery region of the underexpanded source jet column. This flow-acoustic coupling, which leads to resonance in the cavity, was first discovered by Hartmann (1922), where he called these regions in the source jet ‘intervals of instability.’ When the cavity is placed in these intervals, large-amplitude pressure fluctuations are observed at the cavity entrance, along with periodic filling and discharge of fluid in the cavity volume. Although the REM actuator resembles the Hartmann tube or its other adaptations (Kastner and Samimy 2002; Raman and Srinivasan 2009), the resonant frequencies of REM actuators are not predicted by the quarter wave frequency of the cavity. It was hypothesized that the discharge of additional mass through the orifice leads to a modification of the cavity resonance

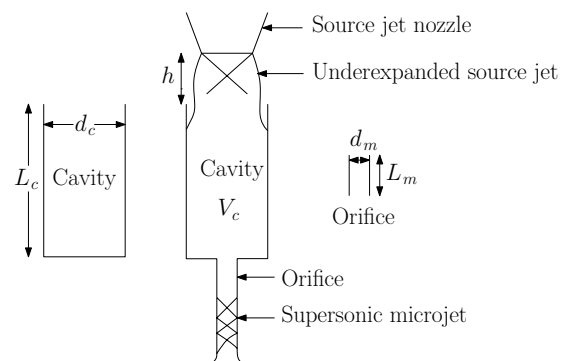


**Fig. 1** Schematic showing the source jet and actuator components. The actuator consists of three components: a source jet, a cavity, and an orifice

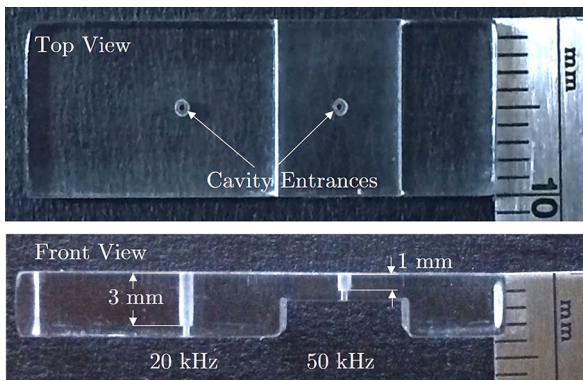


**Fig. 2** Two high-frequency REM actuators, 20 and 50 kHz, fabricated using Plexiglas<sup>TM</sup>. The front view shows two different cavity lengths ( $L_c$ ) for different frequencies

dynamics (Uzun et al. 2011). A lumped element modeling (LEM) approach has been used to design these actuators using the electric circuit analogy. The LEM of these actuators has been discussed in great detail by Solomon (2010) and Solomon et al. (2012). For a single-cavity, single-orifice actuator design, the relation shown in Eq. 1 predicts the fundamental resonant frequency based on acoustic wave propagation in the acoustic elements.

$$f = \frac{c_0}{2\pi} \left[ \left( \frac{S_m l'_c + S_c l'_m}{l'_m l'_c V_c} \right) \left( 1 - \frac{S_m}{S_c} \right) \right]^{1/2} \quad (1)$$

Here,  $c_0$  denotes the ambient acoustic speed, and  $S_c$  and  $S_m$  are the cross-sectional areas of the cavity and orifice, respectively.  $l'_c$  and  $l'_m$  are the effective lengths of the cavity and orifice, respectively, where end corrections for short open tubes (unflanged) have been applied (Blackstock 2000).

In this study, two actuators with nominal frequencies of 20 and 50 kHz were developed and characterized with the goal of implementing high-frequency control on high-speed jets. Since the target frequency ranges were known *a priori*, LEM was used to estimate the actuator dimensions (see Eq. 1). Figure 2 shows the 20 and 50 kHz actuators with cavity lengths of 3 and 1 mm, respectively. The actuators were fabricated using Plexiglas<sup>TM</sup>. The diameter of the microjet orifice was chosen to be 0.4 mm to maintain consistency with previous studies (Arakeri et al. 2003; Alkislar et al. 2007). Some of the other relevant actuator dimensions are presented in Table 1. Since LEM only predicts the most amplified frequency based on acoustic wave propagation, deviations in the actual frequency values from the design frequency is expected, producing a *range of output frequencies*. This will be elaborated upon in Sect. 4.1.

**Table 1** Actuator dimensions associated with high-frequency actuator design

Actuator dimensions/frequencies	20 kHz	50 kHz
Cavity diameter, $d_c$ (mm)	0.8	0.8
Cavity length, $L_c$ (mm)	3	1
Cavity volume, $V_c$ (mm <sup>3</sup> )	1.5	0.5
Orifice length, $L_m$ (mm)	0.5	0.5
Orifice diameter, $d_m$ (mm)	0.4	0.4

## 2.2 Laser-based micro-schlieren system

The length scales associated with the actuators shown in Fig. 2 and Table 1 indicate that the actuator flow field has features on the order of a few hundred microns. To be able to understand the flow dynamics better, a very high spatial and temporal resolution study of the actuator flow fields is required. Therefore, a specialized high-sensitivity, high-magnification laser-based micro-schlieren (LBMS) system was used to resolve the associated micro-time and length scales. The schematic of the LBMS system is shown in Fig. 3.

The schlieren system shown is similar to the one used by Phalnikar et al. (2008). The primary difference is that the current system uses laser-induced breakdown of argon as a broadband light source. Argon increases the spark intensity and decreases the jitter of the spark in the beam direction compared to air discharges (Beutner et al. 2006). The short duration pulse width ( $O(10$  ns)) provided by the laser effectively ‘freezes’ the flow field to allow the imaging of different stages of flow evolution. The laser beam is produced using a New Wave Gemini PIV laser and is focused in an argon atmosphere using an  $f/1.0$ , 25.4 mm plano-convex lens. The laser pulse duration ( $\sim 3$ –5 ns) sustains the plasma for about 10 ns (Volpe and Settles 2006). The light generated is focused on a slit with an  $f/1.4$ , 50-mm camera lens. Light from the slit passes through a  $f/2.4$ , 50.8-mm-diameter plano-convex collimating lens. The resulting parallel beam of light passing through the test section is focused on to a knife edge using another  $f/2.4$ , 50.8-mm-diameter focusing lens. A knife edge is used as a cutoff to increase the sensitivity of the system. An 28–200 mm variable focal length camera lens along with a Kodak Megaplug ES 1.0 camera (1018  $\times$  1018 pixels) were used to acquire the images. The images were acquired using PROVISION<sup>TM</sup> software.

## 2.3 Test conditions and measurements

The experimental setup for acoustic and visual characterizations of the high-frequency REM actuators is shown in

Fig. 4. This setup is placed in the ‘Area of Interest’, in the schlieren schematic shown in Fig. 3. The source jet nozzle, supplied by a compressed nitrogen cylinder, produces the source jet with different underexpansion ratios. The stagnation pressure of the source jet ( $P_0$ ) is measured upstream of the nozzle exit with a 200 PSIG OMEGA steady pressure transducer PX303-200 G5V. The source jet is fitted on to a micro-traverse system that allows for height adjustments. The normalized distance between the source jet and the cavity entrance ( $h/d$ ), and the normalized source jet supply pressure ( $NPR = P_0/P_{amb}$ ) are the two important parameters that determine the actuator frequency. NPR is varied from 5.1 to 9.2 ( $P_0 \sim 60\text{--}120$  psig), and  $h/d$  is varied depending on different locations where the actuator pulses. Microphone measurements were acquired at two locations. The bottom microphone (see Fig. 4) is positioned at a diagonal distance of 40 mm ( $80d$ ) from the actuator orifice exit, and the results are referred to as ‘Acoustic measurement--actuator.’ The top microphone is at a diagonal distance of approximately 50 mm ( $100d$ ) from the actuator cavity entrance. The results from this microphone are denoted as ‘Acoustic measurement---source jet.’ Microphone measurements were acquired using B&K 4939 free-field condenser microphones with B&K 2670 preamplifiers. The signal was conditioned using a B&K model 2960 Nexus amplifier and filtered using a Stanford SR640 low-pass filter set to 100 kHz. All data were acquired using a National Instrument Digital Data Acquisition (DAQ) card (PCI-6133) and a PC using LABVIEW. The signals were sampled at 250 kHz. Narrow band microphone spectra were obtained using FFT lengths of 4096 samples averaged with Hanning window with 75 % overlap.

### 3 Actuator flow field: visual and acoustic study

Detailed benchtop characterizations involving flow visualizations and acoustic measurements of the actuator flow field ( $f = 20$  and 50 kHz, *nominally*) demonstrate their abilities to produce high-amplitude, pulsed supersonic

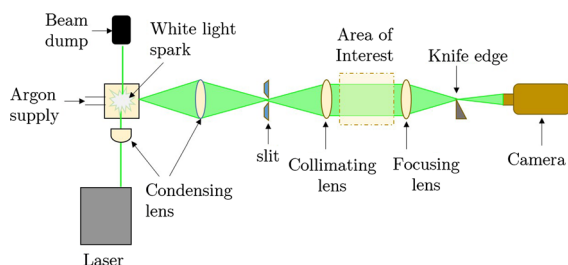


**Fig. 3** Schematic of the laser-based micro-schlieren system showing the laser, test section, lenses, and the camera

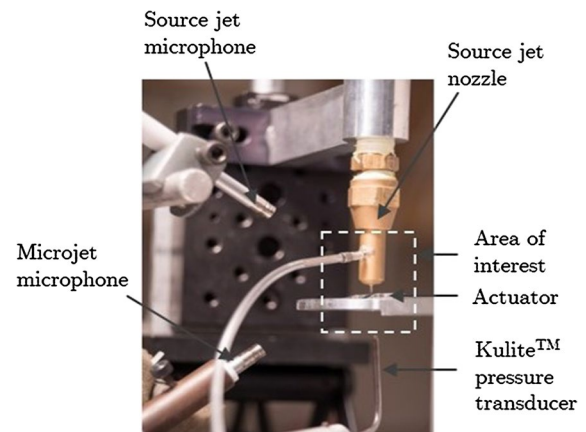


**Fig. 4** Experimental setup of the high-frequency actuators on benchtop for acoustic and visual characterization showing locations of the microphones with respect to the source jet and the actuators

flows at high frequencies. In this section, we present some of these results. First, we present an instantaneous image of the actuator flow field to acquaint the readers with the pertinent features. This is followed by the presentation of some phase-conditioned images and a discussion of the different stages of flow evolution. Flow visualization results are aided by acoustic spectra that show the frequencies and amplitudes of the pulsed flow field.

#### 3.1 REM actuators: flow features

The flow-acoustic coupling between the source jet and the actuator cavity results in resonance in the cavity, producing high-amplitude pressure fluctuations within the cavity and pulsed supersonic microjet with high momentum through the orifice. Under favorable flow and geometric conditions, the microjets pulse at *discrete frequencies*. Figure 5 shows a representative instantaneous schlieren image of the nominally 50-kHz actuator acquired using the LBMS system. This image was acquired at a source jet  $NPR = 9.2$  and  $h/d = 2.0$ . An actuator outline showing the cavity and orifice

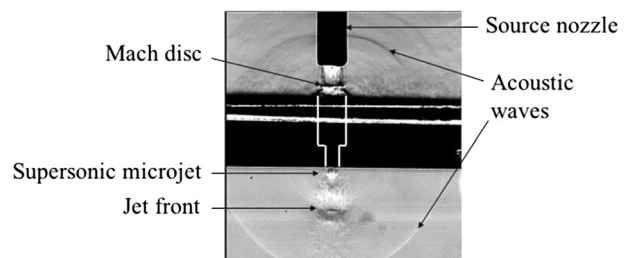


**Fig. 5** Instantaneous micro-schlieren image of the nominally 50 kHz actuator showing important flow features

has been added for clarity. It can be seen from the figure that the underexpanded source jet ( $d = 0.5$  mm) impinges upon the cavity, and a supersonic microjet emanates from the micro-orifice. Acoustic waves in the ambient, a Mach disk in the source jet column near the cavity entrance, and the jet front of the pulsed microjet emanating from the orifice are some of the other prominent features of the actuator flow field that can be observed in Fig. 5. Strong acoustic waves are observed both on the source jet side and the actuator side. A wall jet region, which is more prominent in the 20 kHz actuator flow field, is seen on either side of the cavity entrance as a result of cavity discharge, a phenomena which will be discussed in the context of phase-locked images.

Uzun et al. (2011) performed high-fidelity Large Eddy simulations (LES) to simulate this microscale actuator flow field and provided further insights into the complex physics associated with different stages of flow evolution which are otherwise not observable in experimental configurations. Simulation results show that the actuator frequency corresponds to the frequency of the cavity's periodic filling and discharge process. The filling process is characterized by little-to-no-flow through the orifice, and the discharge stage is characterized by flow spillage from the cavity entrance and a supersonic microjet emanating from the actuator orifice. Details on low frequency ( $\mathcal{O}$  (1 kHz)) REM actuator flow fields have been discussed in considerable detail by Solomon (2010). This paper focuses on characterization of high-frequency REM actuators particularly suited for the control of high-speed flows.

Representative phase-locked images for 20 and 50 kHz (nominally) actuators are presented to show the evolution of the flow field in time. In the images, the former actuator is pulsing at 26.3 kHz at NPR = 8.5 and  $h/d = 1.8$  and the latter is pulsing at 70.9 kHz at NPR = 9.2 and  $h/d = 2.0$ . Figure 6 shows the phase-locked images for the 20 kHz (nominally) actuator. For a pulsing frequency of 26.3 kHz, the period for this actuator is approximately 38  $\mu$ s. A total seven phases are shown, each 6  $\mu$ s (approximately 57°) apart. Phase-conditioned images capture the aforementioned periodic filling and discharge of the cavity as shown in Fig. 6. At what is defined as 0° phase or time  $t = 0$ , a strong supersonic microjet can be seen emanating from the orifice. Additionally, it can be observed that the Mach disk is positioned away from the cavity entrance in the source jet column. This phase represents 'spilling' or discharge from the cavity (see Fig. 6a, b). During the spillage, flow is also discharged from the cavity entrance, pushing the Mach disk away in the source jet column. Furthermore, wall jets are seen on either side of the cavity entrance.

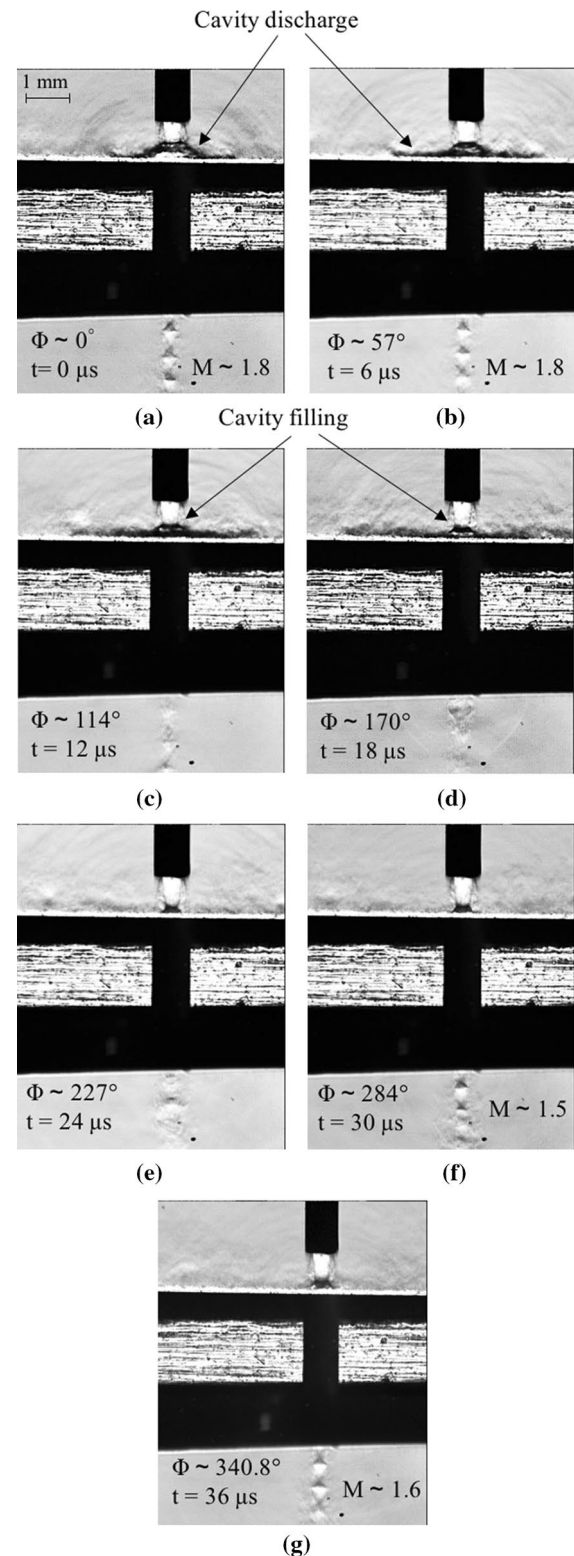
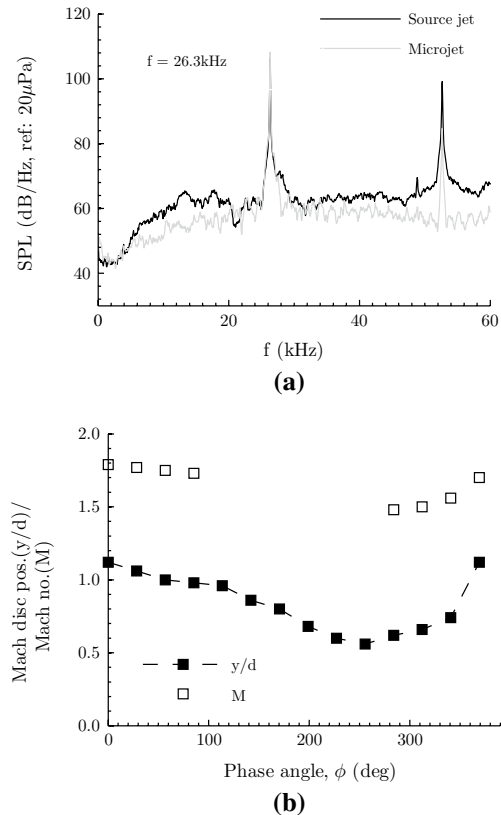


**Fig. 6** Schlieren images for the nominally 20-kHz actuator showing the evolution of flow field in time. The images show the periodic fill-up and discharge of the actuator cavity

As the flow continues to evolve, the Mach disk can be observed to be moving toward the cavity opening as seen in Fig. 6c–e. This represents the ‘filling’ stage. As the Mach disk approaches the cavity entrance, the exit microjet column becomes progressively weaker, leading to a subsonic flow. The flow velocity out of the actuator orifice is near a minimum when the Mach disk is at its lowest position ( $t = 24 \mu\text{s}$ ) as seen in Fig. 6e. This ends the filling process, leading to the completion of one actuator cycle. The actuator begins another cycle when the spilling process restarts and the shock cell structures at the orifice output start reappearing (Fig. 6f), and the Mach disk starts moving away from the cavity entrance. One can notice from Fig. 6d, e that the output velocities from this actuator never completely go to zero but become very low when the Mach disk is closest to the cavity entrance. It can be observed that the position of the Mach disk is correlated with the pulsed microjet emanating out of the orifice; hence, the oscillation of the Mach disk can also be used to characterize the flow unsteadiness near the cavity entrance.

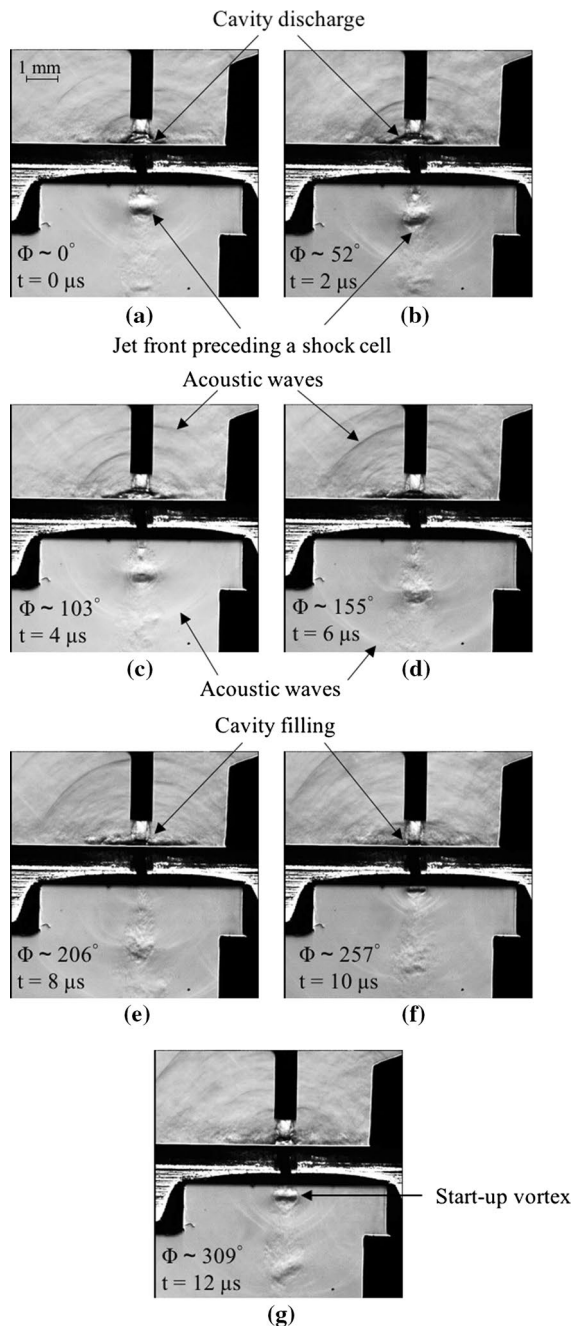
Acoustic data for the source jet and microjet presented in Fig. 7a show the frequency (and its first harmonic) at which the actuator pulses, which appear as distinct peaks. The estimated locations of the Mach disk ( $y$ ) from the cavity entrance, measured from the images, for different phases are normalized with the source jet diameter ( $d$ ) and plotted as a function of phase in Fig. 7b. The intermittent presence of shock cells in the pulsed microjet (at the bottom of the images in Fig. 6) confirms that the output flow is periodically supersonic. Exit Mach numbers of the microjet emanating out of the orifice (for phases with supersonic speeds) have been estimated based on shock cell spacing using the empirical relation by Phalnikar et al. (2008). It should be noted that the estimated Mach numbers correspond to the fully expanded jet Mach numbers. Phases between roughly  $85^\circ$  and  $280^\circ$  represent the subsonic regime (cavity fill stage), where the microjet Mach number could not be estimated. Based on the flow visualizations results, also summarized in Fig. 7b, the duty cycle corresponding to the supersonic/transonic component of the actuator flow is roughly 40–60 %.

Figure 8 shows the phase-locked images for the nominally 50-kHz actuator pulsing at 70.9 kHz for  $\text{NPR} = 9.2$  and  $h/d = 2.0$ . The period of this actuator is very short,  $14 \mu\text{s}$ , and an attempt has been made to ‘freeze’ the flow at every  $1 \mu\text{s}$  increment; seven phases are shown in Fig. 8. As in the previous case, acoustic spectra reveal the global nature of the tones. The high-amplitude nature of pulsing can also be deduced from the energy in the resonant peak, as shown in Fig. 9a. Figure 9b shows the normalized position of Mach disk as a function of phase angle. The nature of temporal evolution of the flow field of the



**Fig. 7** Flow properties of the nominally 20-kHz actuator showing **a** acoustic measurements for the source jet and microjet microphones at  $\text{NPR} = 8.5$  and  $h/d = 1.8$ , **b** measured Mach disk position in the source jet column and the estimated Mach number for microjet as a function of phase angle for a complete cycle

nominally 50-kHz actuator is very similar to that of the previous actuator, although the flow field evolves at a much faster rate. The process of cavity filling/spilling and the concomitant development and decay of supersonic to subsonic microjet velocity out of the orifice can be related to the location of the Mach disk in the source jet column. In the images of this higher frequency actuator, a jet front is always observed to be leading the supersonic jet column, where a shock cell is observed very close to the orifice exit (see Fig. 8a–c). The presence of the jet front in these images is reminiscent of a start-up vortex in pulsed flows and has not been observed previously in REM actuators operating at lower frequencies. The presence of the start-up vortex suggests that the jet starts from a near-zero velocity at the beginning of each cycle. However, due to the very short time associated with the cavity discharge phases, the pulsed microjet flow is only established over a short spatial extent and only one shock cell is observed downstream of the orifice exit. For this reason, the microjet flow Mach numbers could not be estimated for this actuator.



**Fig. 8** Schlieren images for the nominally 50-kHz actuator showing the evolution of flow field in time

### 4 Actuator dynamics

LEM was used to theoretically predict the frequencies of the actuators based on the actuator geometry. In this section, we first compare the observed/actual frequencies of the actuators to the LEM-predicted values. We further explore the performance of these actuators at different operating conditions including off-design conditions (i.e., when the actuator does

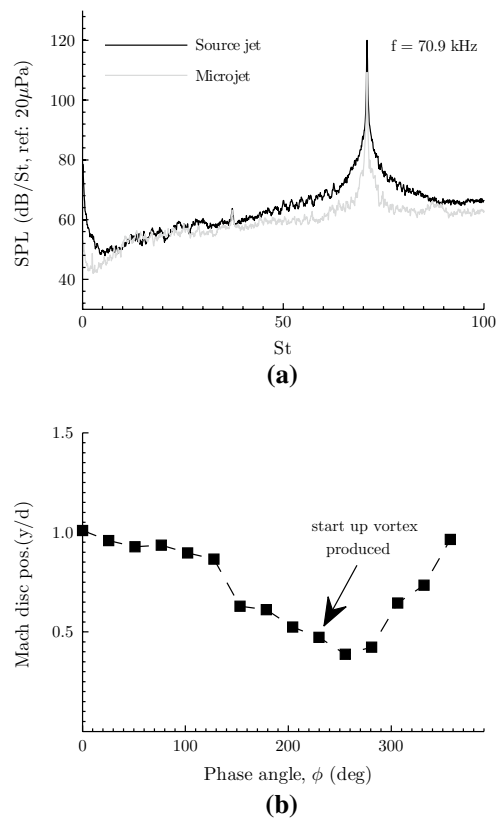


**Fig. 9** Flow properties of the nominally 50-kHz actuator showing **a** acoustic measurements for the source jet and microjet microphones at  $NPR = 9.2$  and  $h/d = 2.0$ , and **b** measured Mach disk position in the source jet column as a function of phase angle for a complete cycle

not produce maximum output). We focus on the aspects that are relevant to the implementation of these actuators in the aforementioned high-speed jet flows.

#### 4.1 LEM prediction and experimental frequencies

REM actuators exploit the flow-acoustic resonance phenomena, where pressure amplification occurs in the cavity when the cavity entrance lies within the pressure recovery region of the source jet. This, for most conditions, produces pulsed supersonic microjets at *discrete frequencies*. LEM predicts the most amplified frequency based solely on acoustic wave propagation in the actuator elements (i.e., cavity or orifice.) and does not account for the flow through them. Varying the input parameters, such as NPR or  $h/d$ , alters the impingement conditions, leading to a deviation from the predicted resonant frequency values. These variations are not captured by LEM very well, if at all. LEM also assumes spatial compactness or negligible spatial variation in pressure ( $\frac{dP}{P} \ll 1$ ) within the acoustic elements. This assumption is not valid as the fluctuation of pressure in the actuator cavity during



**Table 2** Fundamental frequency predicted by LEM versus the measured frequency ranges

Predicted frequency (kHz)	Measured frequencies (kHz)
21.9	20.3–27.8
50.4	54.8–78.2

the actuator fill-up or discharge process is not negligible (Solomon 2010; Uzun et al. 2011). Finally, the current LEM analysis does not allow for correction for losses due to thermo-viscous effects or friction. Due to these reasons, while serving as a very good starting point for REM design, LEM fails to predict the off-design frequency range at which the actuator actually pulses. Table 2 lists the nominal, most amplified frequencies predicted by LEM and the range of measured frequencies for the actuators. It can be noted that for the nominally 20 kHz actuator with  $L_c = 6d = 3$  mm, the measured frequencies differ from the LEM-predicted value by 7–26 %. The nominally 50-kHz actuator with  $L_c = 2d = 1$  mm, on the other hand, has measured frequencies that differ from the predicted frequency by 9–55 %. It appears that for the longer actuator cavity ( $L_c = 6d$ ), cavity resonance dominates the actuator output frequency. However, in the case of the shorter cavity ( $L_c = 2d$ ), the actuator flow field is more sensitive to the changes in boundary conditions (NPR and  $h/d$ ), leading to a wider range of output frequencies. Similar behavior has been observed in other actuators adapted from the Hartman tube (Kastner and Samimy 2002; Raman et al. 2004), where the departure from the quarter wave resonance frequency is observed to be larger for shorter tubes.

Due to our familiarity with LEM and the associated limitations described in the previous paragraph, the deviation in the actual actuator frequencies from theoretical values was anticipated *a priori*. Benchtop studies were performed to measure actuator frequencies at different operating conditions and thus have a quantitative measure of the actuators' tuning range. Details of the aeroacoustic properties that result in the actuator producing a range of frequencies are discussed next.

#### 4.2 Region of instability (ROI) and actuator range of operation

As mentioned in Sect. 2.1, during an investigation of axial pressure distribution in an underexpanded jet column, Hartmann (1922) discovered a periodic fill-up and discharge of the pitot tube when placed in the compression region of the source jet. He termed the compression regions in the underexpanded jet, where pressure recovery takes place, 'intervals of instability.' Solomon (2010) revisited this theory

and designed fluidic actuators with a cavity and microjet orifice(s) with different configurations. Upon traversing the cavity entrance along the pressure recovery region of an underexpanded jet column, strong shock oscillations near the cavity entrance were produced in the source jet, accompanied by high-momentum pulsed microjets expelling out of the actuator orifice.

Based on these studies, the operating range for these HF actuators designed for high-speed flow control applications was analyzed. The pressure recovery regions of the source jet are termed as the Regions of Instability (ROI), to denote the regions where the actuators produce pulsed flow. Figure 10a, b show the variation in the range of  $h/d$  over which an actuator pulses for different values of NPR, for the nominally 20- and 50-kHz actuators, respectively.

As mentioned earlier, the actuator starts to produce pulsed flow when the cavity entrance is placed in the ROI. The open symbols delimit the range where the actuator begins to produce unsteady flow. However, at the extremes of this unsteady flow regime, the unsteady flow field produced by the actuator is primarily broadband. For the interior majority of this interval, the actuator flow field is dominated by *discrete frequency*, high-amplitude *oscillations*; the  $h/d$  values for which this occurs are shown as filled symbols in Fig. 10.

The general trend in Fig. 10 is that the ROI, i.e., the range of  $h/d$  values over which an actuator pulses, grows larger with increasing stagnation pressure (NPR). The first region of instability occurs in the first shock cell downstream of the Mach disk. For a source jet column with a higher NPR, the shock cell spacing increases (Powell 2010), and there is a concomitant increase in the unstable region over which the actuator pulses. Additionally, this stretch also affects the Mach disk position, and hence the upstream position of the first ROI. Finally, for the current actuators tested, all the large-amplitude pulsing occurs within this first pressure recovery region. For some higher values of NPR, the actuators produce unsteady flow fields when placed in the second ROI as well. The amplitude of oscillation, however, was weaker when compared to the one occurring in the first ROI, though these results are not presented here.

For a fixed NPR, the resonant frequency decreases with increasing impingement height ( $h/d$ ) (see Fig. 10), a behavior similar to that of impinging tones (Powell 1988). The actuator produces a highly unsteady flow where the structures in the source jet—shear layer—interact with the cavity. The resonant nature of the flow suggests that the flow field is driven by some sort of feedback loop, but the exact nature of this aeroacoustic resonance is yet unclear and is part of future studies. Some of the details of the intracavity flow field have recently been explored by Uzun

et al. (2011), who clearly demonstrated strong interactions between the flow and acoustics inside as well as in the vicinity of the actuator cavity.

### 4.3 Actuator tunability with variation in operating conditions

In this section, we study the changes in actuator performance, mainly focusing on frequency and amplitude, due to changes in the two primary ‘control knobs’ ( $h/d$  and NPR). The objective is to thoroughly study the actuator behavior for a set of control parameters and assess the potential variation in performance with changes in operating conditions.

#### 4.3.1 Variation in impingement distance ( $h/d$ )

Figure 10 shows wide range of  $h/d$  as a function of varying NPR for which the actuators pulse at *discrete frequencies*. This section discusses two select NPR, 6.4 and 8.5. For the nominally 20 kHz actuator, the spectra for representative

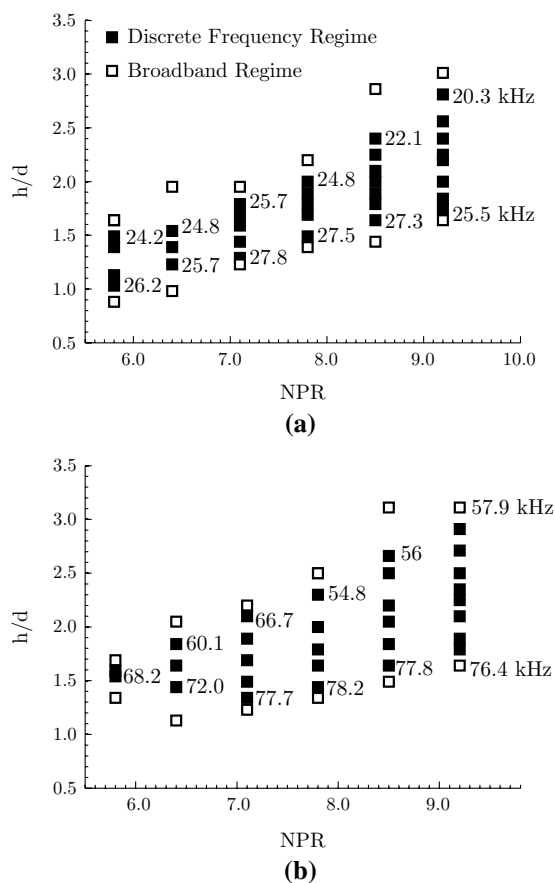


**Fig. 10** Unsteady flow regimes showing the *discrete frequency* regime and the broadband regime for **a** 20-kHz, **b** 50-kHz actuator. Frequencies indicate the limits of strong resonance for each source jet pressure tested

$h/d$  presented in Fig. 11a, b demonstrate the high-frequency high-amplitude flow produced by the actuators for NPR = 6.4 and 8.5, respectively. Figure 11c, d show the estimates of the energy contained within the resonant peaks as well as the total energy measured over the entire spectrum for all  $h/d$  measured, for NPR = 6.4 and 8.5, respectively. The energy within in the resonant peak is calculated by integrating within the frequency range where the power is 25 % of the maximum peak power.

In the above section, we discussed that the actuator has the tendency to pulse at *discrete frequencies* when the cavity entrance is within the ROI. As the actuator encounters the first pressure recovery region (lowest  $h/d$ ), the amplitude of oscillation is smaller and the actuator may not always produce oscillations at discrete frequencies. This is also reflected by low overall energy and low energy in the resonant peak as shown by the representative spectrum for  $h/d = 0.9$  for NPR = 6.4. This amplitude of oscillation increases while the actuator continues to produce pulsed flow at *discrete frequencies* with increasing  $h/d$ . This high-amplitude pulsing occurs until the actuator tends to leave the pressure recovery region of the first shock shell in the source jet. This is shown by the spectra for increasing  $h/d$  in Fig. 11a, b. During the high-amplitude pulsing, it is interesting to note that most of the total energy lies in the resonant peak, as shown by Fig. 11c, d. When the actuator cavity entrance tends to leave the pressure recovery region of the first shock cell, no distinct tones are observed; however, the broadband still remains elevated. These ‘broadband unsteady’ regions of operation have been previously discussed in the context of Fig. 10, where they are shown as open symbols. The overall energy drops when the cavity entrance encounters the regions in the jet column outside the pressure recovery region. As one would expect, the overall energy level is higher for larger source jet NPR values.

Figure 12 shows the spectral plots and energy distributions for two select NPR (6.4 and 8.5) for the nominally 50 kHz actuator. The general trends in spectra and energy remain the same as discussed for the nominally 20-kHz actuator. Upon comparing the measurements for the 50-kHz actuator with that of the 20 kHz, it was observed that the change in frequency with increasing  $h/d$  is consistently larger for the higher-frequency (50 kHz) actuator. Results from parametric study indicate that this variation is not so dramatic for lower NPR values. This can also be noted by comparing results for NPR = 6.4 in Figs. 11a and 12a, where the movement of the peaks appear very similar for both the actuators. However, a larger change in frequency for the 50-kHz actuator, due to changes in  $h/d$ , becomes more evident as the source jet supply pressure or NPR is increased, as can be compared between Figs. 11b and 12b for NPR = 8.5.

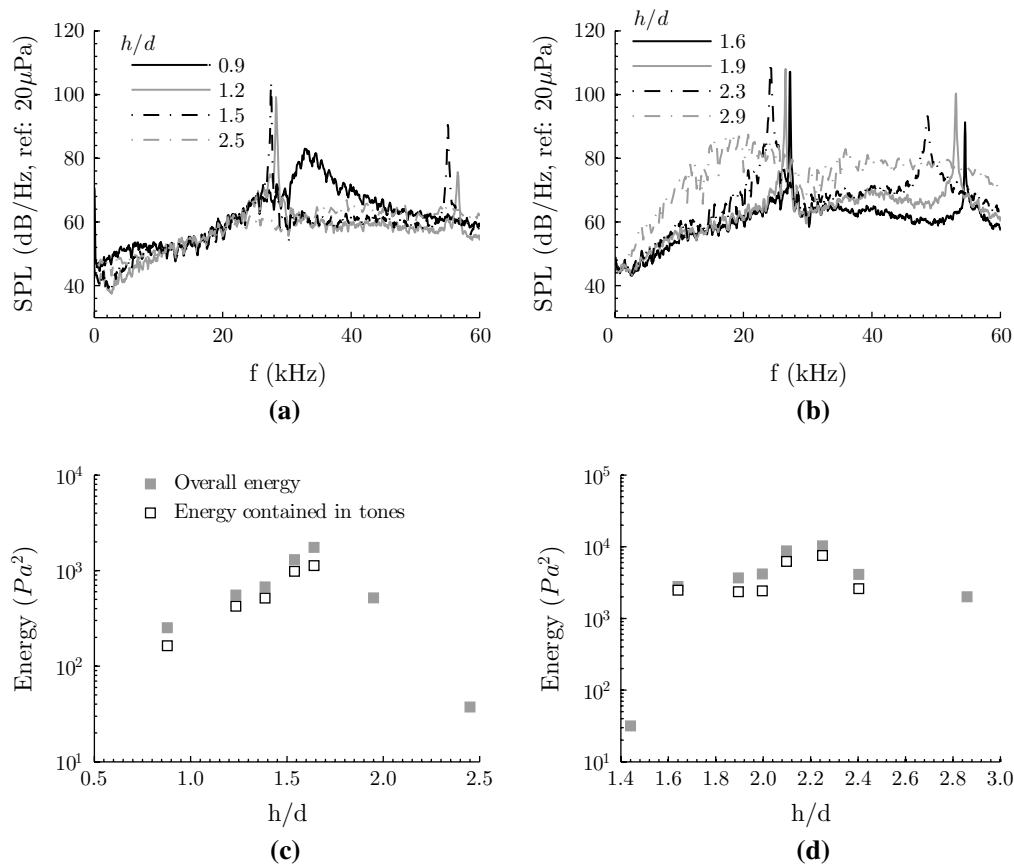


**Fig. 11** Variation in actuator performance with changes in impingement heights for a fixed NPR for the 20-kHz (nominally) actuator showing acoustic spectra for **a** NPR = 6.4, **b** NPR = 8.5, and the variation in energy for **c** NPR = 6.4, **d** NPR = 8.5

#### 4.3.2 Variation in source jet stagnation pressure (NPR)

NPR or the stagnation pressure of the source jet is another significant control knob as it changes the spacing of shock cells, thus shifting the regions over which the actuator can potentially pulse. Figure 13 shows the effect of variation in NPR at a fixed  $h/d$ . Here,  $h/d = 1.8$  and  $2.0$  are selected for the 20- and 50-kHz actuators, respectively, to match the  $h/d$ s with the phase-locked images in Figs. 6 and 8. As demonstrated by flow visualization images (see Fig. 6) and acoustic measurements (see Fig. 7a), the nominally 20-kHz actuator shows high-amplitude pulsing at NPR = 8.5 and  $h/d = 1.8$ . Similarly, the flow field images in Fig. 8 and acoustic results in Fig. 9a show the nominally 50-kHz actuator pulsing at NPR = 9.2 and  $h/d = 2.0$ . A change in NPR for these fixed  $h/d$  changes the frequency as well as the amplitude of pulsing. It can also be observed from Fig. 13 that when NPR is lowered to a certain value (NPR = 6.8 in this case), the actuators no longer resonate at *discrete frequencies*, and the actuator flow fields become *broadband unsteady*. Acoustic spectra for NPR = 6.8 for both actuators exhibit an elevated broadband with no frequency

peaks. As illustrated in Fig. 13, for a fixed impingement height, the actuators pulse at a higher frequency with increasing NPR.

An important conclusion that can be derived from the above results is that the actuators produce high-frequency and high-amplitude outputs for various sets of  $h/d$  and NPR. These results not only provide a measure of the actuators' tuning range, but also reassure their consistent performance for various sets of input parameters. Due to small associated length scales ( $\sim \mathcal{O}(1\text{mm})$ ), slight deviations from the theoretical design brought about by machining and implementation of these actuators become inevitable. Therefore, it is critical for the actuators to have reliable performance over a range of input conditions. Lastly, for the longer cavity ( $L_c = 3\text{ mm}$ ), the deviation of the actual output frequencies from the LEM-predicted value is smaller, whereas for the shorter cavity ( $L_c = 1\text{ mm}$ ), this departure is much larger. This implies that at such small scales ( $\mathcal{O}(1\text{ mm})$ ), a model based purely on acoustic wave propagation is not sufficient to predict the actuator performance for various operating conditions. A better empirical model that incorporates the effect of flow is essential for modeling

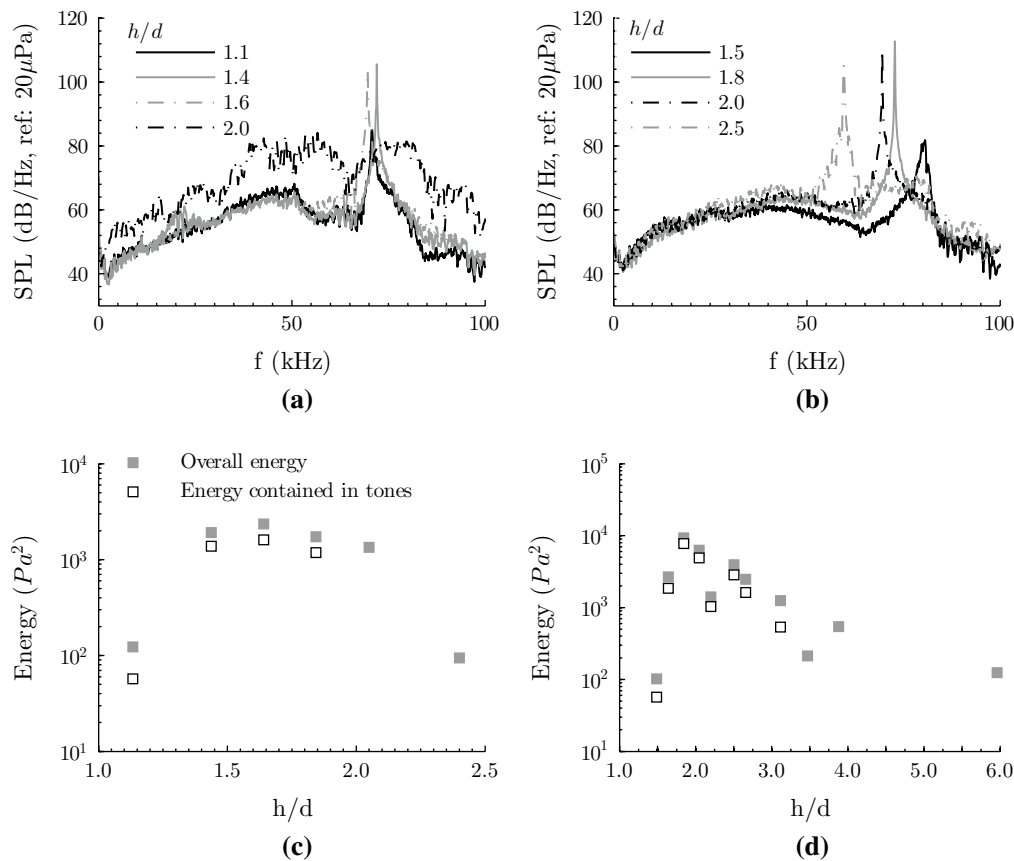


**Fig. 12** Variation in actuator performance with changes in impingement heights for a fixed NPR for the 50-kHz (nominally) actuator showing acoustic spectra for **a** NPR = 6.4, **b** NPR = 8.5, and variation in energy for **c** NPR = 6.4, **d** NPR = 8.5

these actuators. This will be a part of future studies. Nonetheless, acoustic measurements and flow visualization of these actuators show promising results in terms of the dynamic response and control authority, demonstrating their potential in high-speed flow control.

## 5 HF-REM actuators: preliminary implementation

This section briefly summarizes the results from the implementation of the nominally 20-kHz actuator on a Mach 0.9 ( $Re_D = 6 \times 10^5$ ) free jet. First, the actuator design for this implementation is presented. This is followed by some results involving the effect of actuation on the near-field jet acoustics. Preliminary flow and acoustic results showing the effect of high-frequency forcing on the mean and turbulent characteristics of the jet is presented in Upadhyay et al. (2016). This paper only presents limited near-field acoustic results to show the potential of these actuators in jet noise control. Detailed analysis of the mechanisms associated with high-frequency control and its effect on

the evolution of large-scale structures will be a part of future studies.

### 5.1 Actuator design for free jet implementation

For implementation of the HF-REM actuators in the free jet flow field, the simple actuator design shown in Fig. 2 was modified. The actuator and source jet pieces are capable of sliding on a dovetail rail for  $h/d$  adjustments. The actuator–source jet configuration is shown in Fig. 14a, b. The configuration consists of 1/4 in. internal diameter stainless steel tubes bent at  $60^\circ$  which support the actuator assemblies. The tube also serves as a secondary pressure reservoir and supplies compressed nitrogen to the source jet through soldered copper tubing. Nitrogen is supplied to the tube configuration by a primary stagnation chamber consisting of a 1-in.-inner-diameter stainless steel tube formed into a ring with a 12 in. outer diameter. Nitrogen at 100 psig is supplied to the primary stagnation chamber from compressed gas cylinders. A pressure tap in one of the 1/4-in. actuator tubes allows for the measurement of stagnation pressure during actuator operation. Eight actuators are azimuthally

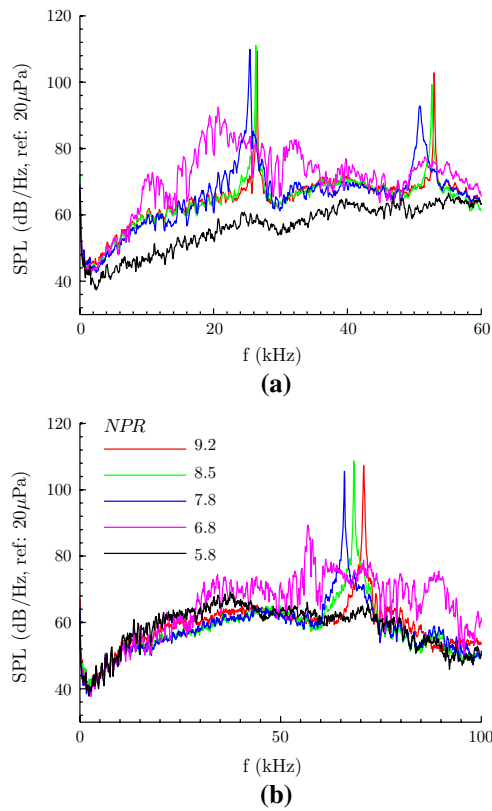


**Fig. 13** Acoustic spectra showing actuator performance at different NPR for a fixed  $h/d$  for **a** 20-kHz (nominally) actuator for an  $h/d = 1.8$ , **b** 50-kHz (nominally) actuator for an  $h/d = 2.0$

distributed around the nozzle exit so that the resulting microjets penetrate the shear layer at an angle of  $60^\circ$ , as shown in Fig. 14b. This angle was selected based on optimization studies for noise reduction performed in the past (Greska 2005; Lou 2005). Figure 14c shows the final setup with the primary stagnation chamber and eight actuator assemblies azimuthally distributed at the nozzle exit. Prior to implementation, each actuator was individually characterized on the benchtop using the same acoustic and visual techniques used for the prototype actuators shown in Fig. 2.

### 5.2 Test conditions and measurements

Experiments involving the implementation of the actuators on a Mach 0.9 free jet flow field were performed at the STOVL high-speed jet facility at FCAAP. This is a blow-down facility which can simulate flow-induced effects in both impinging and free jet configurations. Details on the facility can be found in Wiley (2010). For the work presented here, a converging axisymmetric nozzle is used to run an ideally expanded Mach 0.9 jet with  $P_0/P_{amb} = 1.69$  and  $T_0/T_{amb} \approx 1.0$ . The nozzle is designed using

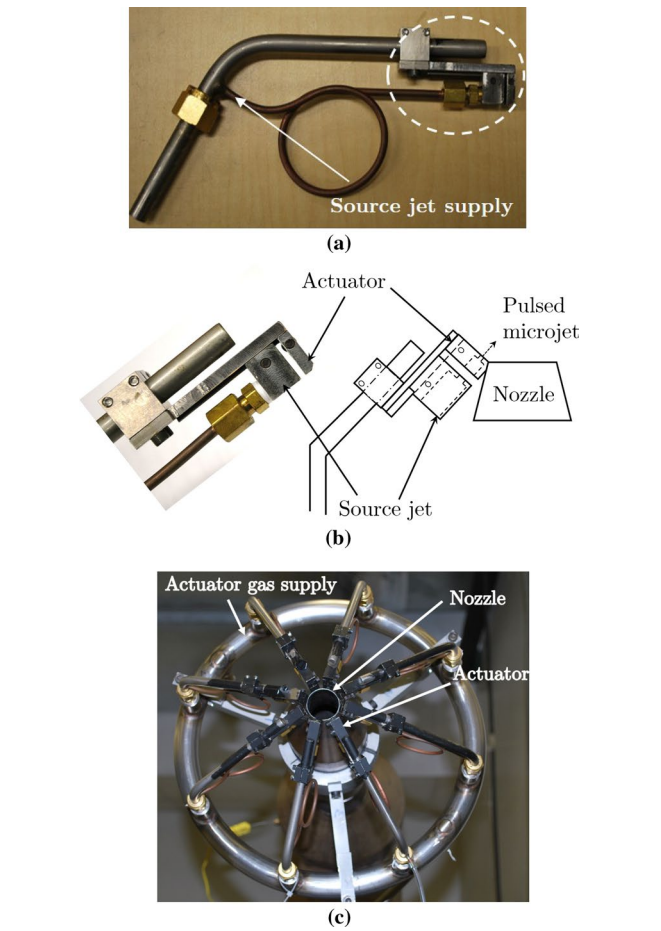


**Fig. 14** Implementation of REM actuators on a Mach 0.9 jet showing **a** individual actuator assembly with source jet, actuator, and source jet supply, **b** detailed schematic of the actuator showing the orientation at the nozzle exit, **c** final actuator assembly showing the actuator manifold with stagnation ring and the nozzle

fifth-order polynomial converging to an exit diameter of  $D = 25.4$  mm.

Microphone measurements were conducted in the jet near field to assess the effect of high-frequency control on the near-field acoustics. Acoustic measurements were performed using B&K 4939 free-field condenser microphones equipped with B&K 2670 preamplifiers and powered by a B&K model 2690 Nexus amplifier. A linear array of microphones was placed in the jet near field,  $15D$  from the jet axis. The array consisted of 7 microphones placed every  $10^\circ$  between  $90^\circ$  and  $150^\circ$ , as measured from the jet inlet axis. Data were acquired using a National Instruments Digital Data Acquisition (DAQ) card (NI PCI-4472) and a PC running LABVIEW software. The signals were simultaneously sampled at 80 kHz. Narrowband microphone spectra were obtained using an FFT length of 4096 samples with a Hanning window and 75 % overlap. Although most of the

objects in close proximity of the jet are acoustically treated during the test, the facility is not anechoic. The acoustic results, however, satisfy our objective of comparing baseline noise levels to that with control in the near field.

### 5.3 Acoustic properties

The primary goal of high-frequency forcing is to reduce turbulent mixing noise due to large-scale structures that are known to be the most dominant source of noise in high-speed jets. A modification in the evolution of these large-scale structures is manifested in the noise levels of the jet. To demonstrate the influence of control on the near-field noise, acoustic spectra at  $90^\circ$  and  $150^\circ$  are presented in Fig. 15. Results from these two angles are representative of the two extremes of the directivity curve (see Fig. 16) and are in agreement with the acoustic measurements for turbulent jets in the literature (Tam 1998). The spectra for  $90^\circ$  mic is relatively flat and is typical of acoustic radiation in the sideline angles. Highly directional noise due to large-scale structures in the downstream shear layer dominates the spectra at  $150^\circ$ . Figure 15b shows that the spectra peaks at approximately  $St = 0.22$  for  $150^\circ$ , followed by a steep spectral decay for higher Strouhal numbers. This behavior is consistent with the observations for high-speed jets where the peak occurs at around  $St = 0.2$  (Viswanathan 2002; Morris 2009).

Acoustic spectra with control are characterized by the actuation tone at approximately  $St_D = 2.2$  (25 kHz). Reduction is observed at low Strouhal numbers for both polar angles up to a crossover frequency associated with the actuator frequency. The maximum SPL reduction for the  $90^\circ$  mic is 3.4 dB, which is observed at  $St_D = 0.6$ . For the peak noise radiation angle of  $150^\circ$ , a reduction of 2.6 dB was observed at  $St_D = 0.22$ . Apart from the acoustic benefit at low frequencies, an increase in high-frequency noise due to the actuator's resonant frequency is noted after a crossover Strouhal number of approximately 1.8 (20 kHz). Unlike passive mixers that exhibit a signature high-frequency lift ( $St \leq 1$ ), no significant increase in noise levels besides the actuation peak is observed in case of present high-frequency excitation (Alkislar et al. 2007). This indicates that localized, high-frequency injection at the nozzle exit has influenced the initial shear layer, resulting in the suppression of the acoustically dominant large-scale structures, without adding to the high-frequency broadband.

The acoustic measurements are also used to calculate the jet directivity. It is evident from the control spectra shown in Fig. 15 that the calculated OASPL will be influenced by the frequency peak when actuator noise becomes dominant. In order to isolate the effect of control

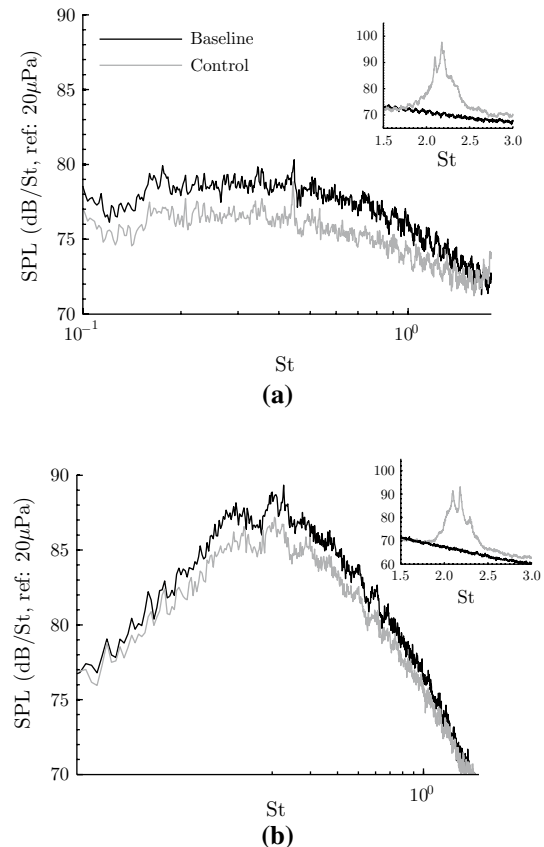


**Fig. 15** Acoustic spectra for a Mach 0.9 jet with and without high-frequency actuation showing measurements from **a**  $90^\circ$  mic, **b**  $150^\circ$  mic. *Inset* Increase in high-frequency noise due to actuator frequency. The crossover Strouhal number ( $St_D \approx 1.8$ ) coincides with the onset of the actuator peak

on the low-frequency noise, OASPL is calculated by integrating the power spectral density over a Strouhal number range from  $St = 0.0$  to  $St = 1.8$ . Reductions of approximately 1.8 and 1.6 dB are observed at  $90^\circ$  and  $150^\circ$ , respectively. Moreover, using this approach, it is interesting to note that high-frequency excitation results in decibel reduction across all polar angles, as illustrated by Fig. 16. This suppression of the low-frequency noise suggests a modification of the acoustically significant large-scale structures in the jet. These structures ( $l/D \sim \mathcal{O}(1)$ ) are mainly responsible for low-frequency noise. Hence, the observed reductions at low- to moderate-frequencies show potential of high-frequency actuators in reducing dominant noise due to large-scale structures. Detailed investigations of the changes in acoustic characteristics of the jet will be performed with far-field measurements in the future.

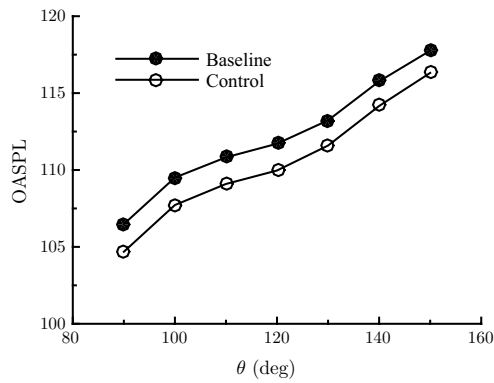


**Fig. 16** Directivity showing reductions in OASPL levels across all polar angles. OASPL is calculated between  $St = 0$  and  $St = 1.8$

## 6 Concluding remarks

The work presented discusses the development and characterization of two high-frequency REM actuators (20 and 50 kHz, nominally) for high-speed jet noise control. To our knowledge, the present study is the first demonstration of such high-frequency capabilities with a fluidic actuator design that is simple and easy to integrate and yet provides a high control authority over a range of high frequencies. For various sets of supply pressures and impingement heights tested, the nominally 20- and 50-kHz actuators were shown to produce supersonic microjets at a range of frequencies, 20.3–27.8 and 54.8–78.2 kHz, respectively. The larger departure of the measured frequency range from the LEM-predicted value, for the smaller actuator cavity, indicates that the higher-frequency actuator (50 kHz) is more sensitive to the effect of flow and boundary condition changes (NPR and  $h/d$ ). Therefore, a better empirical model suited particularly for high-frequency actuators is needed. Implementation of the nominally 20-kHz actuator on a Mach 0.9 free jet flow field shows promise in terms of reducing noise due to large-scale structures. A uniform reduction in the near-field noise for all observation angles was obtained. Detailed investigations on the mechanisms associated with high-frequency control and its effect on the shear layer and turbulence characteristics of the jet will be undertaken in future.

## References

- Ahuja K, Blakney D (1985) Tone excited jets, part IV: acoustic measurements. *J Sound Vib* 102(1):93–117
- Alkislar MB, Krothapalli A, Butler G (2007) The effect of streamwise vortices on the aeroacoustics of a mach 0.9 jet. *J Fluid Mech* 578:139–169
- Arakeri V, Krothapalli A, Siddavaram V, Alkislar M, Lourenco L (2003) On the use of microjets to suppress turbulence in a mach 0.9 axisymmetric jet. *J Fluid Mech* 490:75–98

- Armstrong RR, Michalke A, Fuchs HV (1977) Coherent structures in jet turbulence and noise. *AIAA J* 15(7):1011–1017
- Bechert D, Pfizenmaier E (1975) On the amplification of broad band jet noise by a pure tone excitation. *J Sound Vib* 43(3):581–587
- Beutner TJ, Adelgren R, Elliott G (2006) Characterization of schlieren light source using laser-induced optical breakdown in argon. *AIAA J* 44(2):399–402
- Blackstock DT (2000) *Fundamentals of physical acoustics*. Wiley, London
- Cattafesta LN III, Sheplak M (2011) Actuators for active flow control. *Annu Rev Fluid Mech* 43:247–272
- Cavaliere AV, Rodríguez D, Jordan P, Colonius T, Gervais Y (2013) Wavepackets in the velocity field of turbulent jets. *J Fluid Mech* 730:559–592
- Crow SC, Champagne F (1971) Orderly structure in jet turbulence. *J Fluid Mech* 48(03):547–591
- Fuchs HV, Michel U (1978) Experimental evidence of turbulent source coherence affecting jet noise. *AIAA J* 16(9):871–872
- Greska BJ (2005) *Supersonic jet noise and its reduction using micro-jet injection*. PhD dissertation, Florida State University, ProQuest Dissertations Publishing, 3183064
- Hartmann J (1922) On a new method for the generation of sound-waves. *Phys Rev* 20(6):719
- Hussain A, Hasan M (1985) Turbulence suppression in free turbulent shear flows under controlled excitation. Part 2. Jet-noise reduction. *J Fluid Mech* 150:159–168
- Jordan P, Colonius T (2013) Wave packets and turbulent jet noise. *Annu Rev Fluid Mech* 45:173–195
- Kastner J, Samimy M (2002) Development and characterization of Hartmann tube fluidic actuators for high-speed flow control. *AIAA J* 40(10):1926–1934
- Kibens V (1980) Discrete noise spectrum generated by acoustically excited jet. *AIAA J* 18(4):434–441
- Krothapalli A, Venkatakrishnan L, Lourenco L, Greska B, Elavarasan R (2003) Turbulence and noise suppression of a high-speed jet by water injection. *J Fluid Mech* 491:131–159
- Kuo CW, Morris P, McLaughlin DK (2012) Noise reduction in supersonic jets by nozzle fluidic inserts. In: 18th AIAA/CEAS aeroacoustics conference (33rd AIAA Aeroacoustics Conference), American Institute of Aeronautics and Astronautics
- Laurendeau E, Bonnet JP, Jordan P, Delville J et al (2006) Impact of fluidic chevrons on the turbulence structure of a subsonic jet. *AIAA Pap* 3510:2006
- Lou H (2005) *Control of supersonic impinging jets using microjets*. PhD dissertation, Florida State University, ProQuest Dissertations Publishing, 3183086
- Michalke A (1977) Instability of a compressible circular free jet with consideration of the influence of the jet boundary layer thickness. *NASA-TM-75190*
- Michalke A (1984) Survey on jet instability theory. *Prog Aerosp Sci* 21:159–199
- Mollo-Christensen E (1963) Measurements of near field pressure of subsonic jets. Tech. rep, DTIC Document
- Mollo-Christensen E (1967) Jet noise and shear flow instability seen from an experimenters viewpoint. *J Appl Mech* 34(1):1–7
- Moore C (1977) The role of shear-layer instability waves in jet exhaust noise. *J Fluid Mech* 80(02):321–367
- Morris PJ (2009) A note on noise generation by large scale turbulent structures in subsonic and supersonic jets. *Int J Aeroacoust* 8(4):301–315
- Phalnikar K, Kumar R, Alvi F (2008) Experiments on free and impinging supersonic microjets. *Exp Fluids* 44(5):819–830
- Powell A (1988) The sound-producing oscillations of round under-expanded jets impinging on normal plates. *J Acoust Soc Am* 83(2):515–533

- Powell A (2010) On Prandtl's formulas for supersonic jet cell length. *Int J Aeroacoust* 9(1):207–236
- Raman G, Srinivasan K (2009) The powered resonance tube: from Hartmann's discovery to current active flow control applications. *Prog Aerosp Sci* 45(4):97–123
- Raman G, Khanafseh S, Cain A, Kerschen E (2004) Development of high bandwidth powered resonance tube actuators with feedback control. *J Sound Vib* 269(3):1031–1062
- Reba R, Narayanan S, Coloni T (2010) Wave-packet models for large-scale mixing noise. *Int J Aeroacoust* 9(4–5):533–558
- Samimy M, Kim JH, Kastner J, Adamovich I, Utkin Y (2007) Active control of a mach 0.9 jet for noise mitigation using plasma actuators. *AIAA J* 45(4):890–901
- Samimy M, Kim JH, Kearney-Fischer M, Sinha A (2010) Acoustic and flow fields of an excited high Reynolds number axisymmetric supersonic jet. *J Fluid Mech* 656:507–529
- Solomon JT (2010) High-bandwidth unsteady microactuators for active control of high-speed flows. Florida State University
- Solomon JT, Foster C, Alvi FS (2012) Design and characterization of high-bandwidth, resonance enhanced pulsed microactuators: a parametric study. *AIAA J* 51(2):386–396
- Tam CK (1998) Jet noise: since 1952. *Theoret Comput Fluid Dyn* 10(1–4):393–405
- Tam CK, Viswanathan K, Ahuja K, Panda J (2008) The sources of jet noise: experimental evidence. *J Fluid Mech* 615:253–292
- Upadhyay P, Valentich G, Alvi FS (2016) Flow and acoustic features of a mach 0.9 jet using high frequency excitation. In: 54th AIAA Aerospace Sciences Meeting, p 0527
- Uzun A, Hussaini MY (2011) Prediction of noise generated by a round nozzle jet flow using computational aeroacoustics. *J Comput Acoust* 19(03):291–316
- Uzun A, Foster CH, Solomon JT, Oates WS, Hussaini MY, Alvi FS (2011) Simulations of pulsed actuators for high-speed flow control. In: Proceedings of the 17th AIAA/CEAS aeroacoustics conference, Portland, Oregon
- Viswanathan K (2002) Analysis of the two similarity components of turbulent mixing noise. *AIAA J* 40(9):1735–1744
- Vlasov E, Ginevskii A, Karavosov R, Makarenko T (1999) Turbulence suppression in subsonic jets by high-frequency acoustic excitation. *Fluid Dyn* 34(1):23–28
- Volpe JA, Settles GS (2006) Laser-induced gas breakdown as a light source for schlieren and shadowgraph particle image velocimetry. *Opt Eng* 45(8):080509–080509
- Wiley AS (2010) Effects of unsteady actuation on resonance-dominated impinging jets. Florida State University
- Worden TJ, Upadhyay P, Gustavsson JP, Alvi FS (2014) Studies on microjet control effectiveness in high-temperature supersonic impinging jets. *AIAA J* 52(8):1757–1769
- Zaman K (1985) Far-field noise of a subsonic jet under controlled excitation. *J Fluid Mech* 152:83–111
- Zaman K, Hussain A (1981) Turbulence suppression in free shear flows by controlled excitation. *J Fluid Mech* 103:133–159
- Zhuang N, Alvi FS, Alkisar MB, Shih C (2006) Supersonic cavity flows and their control. *AIAA J* 44(9):2118–2128